

Auto-AD: Autonomous Hyperspectral Anomaly Detection Network Based on Fully Convolutional Autoencoder

Shaoyu Wang[✉], Student Member, IEEE, Xinyu Wang[✉], Liangpei Zhang[✉], Fellow, IEEE,
and Yanfei Zhong[✉], Senior Member, IEEE

Abstract—Hyperspectral anomaly detection is aimed at detecting observations that differ from their surroundings, and is an active area of research in hyperspectral image processing. Recently, autoencoders (AEs) have been applied in hyperspectral anomaly detection; however, the existing AE-based methods are complicated and involve manual parameter setting and preprocessing and/or postprocessing procedures. In this article, an autonomous hyperspectral anomaly detection network (Auto-AD) is proposed, in which the background is reconstructed by the network and the anomalies appear as reconstruction errors. Specifically, through a fully convolutional AE with skip connections, the background can be reconstructed while the anomalies are difficult to reconstruct, since the anomalies are relatively small compared to the background and have a low probability of occurring in the image. To further suppress the anomaly reconstruction, an adaptive-weighted loss function is designed, where the weights of potential anomalous pixels with large reconstruction errors are reduced during training. As a result, the anomalies have a higher contrast with the background in the map of reconstruction errors. The experimental results obtained on a public airborne data set and two unmanned aerial vehicle-borne hyperspectral data sets confirm the effectiveness of the proposed Auto-AD method.

Index Terms—Adaptive-weighted loss, autonomous detection, fully convolutional autoencoder (AE), hyperspectral anomaly detection.

I. INTRODUCTION

HYPERSPECTRAL imaging provides rich spectral information, which makes it possible to precisely distinguish different materials [1]–[4]. Hyperspectral anomaly detection is one of the most important research fields of hyperspectral information processing and has drawn much attention over the

Manuscript received May 4, 2020; revised August 31, 2020, November 27, 2020, and December 31, 2020; accepted January 3, 2021. This work was supported in part by the National Key Research and Development Program of China under Grant 2017YFB0504202, in part by the National Natural Science Foundation of China under Grant 41771385 and Grant 42071350, and in part by the Postdoctoral Research Foundation of China. (Corresponding authors: Xinyu Wang; Yanfei Zhong.)

Shaoyu Wang, Liangpei Zhang, and Yanfei Zhong are with the State Key Laboratory of Information Engineering in Surveying, Mapping and Remote Sensing, Wuhan University, Wuhan 430079, China, and also with the Hubei Provincial Engineering Research Center of Natural Resources Remote Sensing Monitoring, Wuhan University, Wuhan 430072, China (e-mail: wangshaoyu@whu.edu.cn; zlp62@whu.edu.cn; zhongyanfei@whu.edu.cn).

Xinyu Wang is with the School of Remote Sensing and Information Engineering, Wuhan University, Wuhan 430072, China (e-mail: wangxinyu@whu.edu.cn).

Color versions of one or more figures in this article are available at <https://doi.org/10.1109/TGRS.2021.3057721>.

Digital Object Identifier 10.1109/TGRS.2021.3057721

years. The hyperspectral anomaly detection task is aimed at detecting observations with significant differences in spectral characteristics with their neighboring background [5], [6]. Such observations are referred to as anomalies. Since there is no prior knowledge available for anomalies [7], background estimation is the crucial step in hyperspectral anomaly detection [8]–[10].

In the early stage of anomaly detection, the hyperspectral data were assumed to obey a certain statistical distribution, and statistical variables were calculated for the background estimation. The Gaussian multivariate distribution is the most commonly used distribution, based on which a lot of methods have been proposed. The Reed–Xiaoli (RX) detector [11] assumes that the background obeys a Gaussian multivariate distribution, and a covariance matrix is calculated for the background estimation. Inspired by the RX detector, some improved methods have also been developed based on a multivariate normal distribution, including the kernel RX-algorithm [12], the linear-filter-based RX detector [13], and the blocked adaptive computationally efficient outlier nominator (BACON) detector [14]. However, as real hyperspectral data are more complicated than a Gaussian multivariate distribution, the random-selection-based anomaly detector (RSAD) [15] assumes that the background obeys a chi-squared distribution, and uses subsets of the background pixels to compute robust background statistics which present a robust representation of the background. However, in these statistical-based methods, their statistical distribution assumptions are often not ideal when considering scenes with complicated land-cover distributions [16].

To deal with the statistical distribution assumptions, image priors, such as sparsity and low-rank priors, have been introduced into hyperspectral anomaly detection [17]–[22]. For example, Li *et al.* [17] proposed a background joint sparse representation detection (BJSRD) method, which assumes that each pixel can be compactly represented by only a few coefficients in a certain basis or dictionary. Recently, Li *et al.* [18] proposed a collaborative-representation-based detector (CRD), based on the concept that each pixel belonging to the background can be approximately represented by its neighboring pixels, while the anomalies cannot.

Since the background can be approximately represented by a set of basis background signals, the low-rank prior has been applied in hyperspectral anomaly detection for background

estimation. Typical examples include the low-rank and sparse matrix decomposition (LRaSMD)-based Mahalanobis distance method (LSMAD) [19], the anomaly detection method based on low-rank and sparse representation (LRASR) [20], and the abundance- and dictionary-based low-rank decomposition (ADLR) [21] method. These representation-based methods formulate the hyperspectral anomaly detection as an energy minimization problem [23]. In this case, regularization parameters are introduced, which need to be manually set [24]. However, the regularization parameters can be difficult to determine since no prior knowledge about the anomalies is available. On the other hand, image priors are often not ideal for use with real hyperspectral data [25], [26].

Recently, autoencoders (AEs) have been applied in hyperspectral anomaly detection [27]–[31] as AEs can learn hierarchical, abstract, and high-level representations of hyperspectral data. For example, a spectral constrained adversarial AE (SC_AAE) was proposed by Xie *et al.* [31], in which a spectral constraint strategy is incorporated into an adversarial AE to learn the latent representation of the preprocessed hyperspectral data, and then a bi-layer architecture is used to realize anomaly detection. By combining manifold learning and an AE, a manifold-constrained AE network was proposed for anomaly detection by Lu *et al.* [30]. In this method, manifold learning is first performed to obtain the embedding representation, which constrains the learning of the AE. Finally, the overall reconstruction error, consisting of both the global and local reconstruction errors, is utilized for the anomaly detection. Stacked denoising AEs (SDAs) have also been introduced into hyperspectral anomaly detection [28], in which the original image is preprocessed by principal component analysis (PCA) and whitening, and then SDA is utilized for the extraction of latent features. Although representations learned by AEs are useful for background estimation, the existing AE-based methods are complicated, and require parameters to be manually set, in addition to pre-processing or post-processing procedures, e.g., the dimension of the embedding manifold [28] or the number of principal components [26].

In this article, an autonomous hyperspectral anomaly detection network (Auto-AD) is proposed, in which the background is reconstructed by the network and the anomalies appear as reconstruction errors. Specifically, the background is reconstructed via a fully convolutional AE with skip connections, considering that a great deal of image statistics can be captured by the structure of a convolutional image generator for hyperspectral images [25]. On the other hand, anomalies are difficult to reconstruct with the network because anomalies are relatively small compared to the background and only occur in the image with a low probability, thus appearing as reconstruction errors. As a result, large reconstruction errors indicate potential anomalous pixels. However, the anomalies still have a low probability of being reconstructed. To further suppress the anomaly reconstruction, an adaptive-weighted loss function is designed, where the weights of the potential anomalous pixels are reduced for the total loss. The weights are adaptively updated during training since they are derived from the reconstruction errors.

The main contributions of this article can be summarized as follows.

- 1) A novel hyperspectral anomaly detection framework based on a fully convolutional AE is proposed. Specifically, the background is reconstructed with the same dimensionality as the original image, to avoid loss of spectral information, while the anomalies are detected based on reconstruction errors, to avoid the construction of additional detectors.
- 2) The proposed Auto-AD method achieves autonomous hyperspectral anomaly detection. Furthermore, the Auto-AD method does not require any parameters to be manually set, and involves no pre-processing or post-processing procedures. Owing to the ability of the proposed network to accurately reconstruct the background, the anomalies are automatically separated.
- 3) An adaptive-weighted loss function is proposed to further suppress the anomaly reconstruction, in which the weights of potential anomalous pixels are reduced during training. Thus, anomalies have a higher contrast with the background in the map of reconstruction errors. The weights are adaptively updated since they are derived from the reconstruction errors.

The rest of this article is organized as follows. Section II gives a brief introduction to the related work. Section III provides a detailed description of the proposed method. Section IV describes the data sets and analyzes the experimental results. Finally, our conclusions are drawn in Section VI.

II. RELATED WORK

In this section, we briefly introduce the classic RX detector and the anomaly detection method based on LRASR. As the proposed method is based on an AE, the basic principle of AEs is also described in this section.

A. Reed-Xiaoli Detector

Suppose that \mathbf{x} represents the pixel vector, the RX detector [11] is given by

$$D(\mathbf{x}) = (\mathbf{x} - \boldsymbol{\mu})^T \mathbf{C}^{-1} (\mathbf{x} - \boldsymbol{\mu}) \quad (1)$$

where $\boldsymbol{\mu}$ is the sample mean, \mathbf{C} is the sample covariance matrix of the image, and N represents the total number of pixels

$$\begin{aligned} \boldsymbol{\mu} &= \frac{1}{N} \sum_{i=1}^N \mathbf{x}_i \\ \mathbf{C} &= \frac{1}{N} \sum_{i=1}^N (\mathbf{x}_i - \boldsymbol{\mu})(\mathbf{x}_i - \boldsymbol{\mu})^T. \end{aligned} \quad (2)$$

B. Low-Rank and Sparse Representation

The LRASR method [20] utilizes the low-rank prior of the background and the sparse prior of the anomalies in the hyperspectral imagery. The hyperspectral data matrix \mathbf{X} can then be split into a background part and an anomalous part

$$\mathbf{X} = \mathbf{DS} + \mathbf{E} \quad (3)$$

where \mathbf{D} is the background dictionary, which is composed of the background samples; and \mathbf{S} is the representation coefficients. \mathbf{DS} denotes the background part and \mathbf{E} denotes the anomalous part. The anomalous part \mathbf{E} is then optimized by solving the following energy minimization problem:

$$\min_{\mathbf{S}, \mathbf{E}} \|\mathbf{S}\|_* + \lambda \|\mathbf{E}\|_{2,1} \quad \text{s.t. } \mathbf{X} = \mathbf{DS} + \mathbf{E} \quad (4)$$

where $\|\cdot\|_*$ denotes the matrix nuclear norm and $\|\cdot\|_{2,1}$ denotes the matrix $l_{2,1}$ -norm. λ is the regularization parameter, which has to be manually set. However, this parameter is difficult to determine since no *a priori* knowledge about the anomalies or background is available. In addition, the low-rank prior is too strong for the complicated background of real hyperspectral data.

C. Autoencoders

An AE [32]–[34] is a feed-forward artificial neural network which is composed of an encoder and a decoder. The parameters of the network, including the weights and bias, are estimated by the back-propagation method [35]. The encoder is used to learn a mapping from the input layer \mathbf{x} to the hidden layer \mathbf{y}

$$\mathbf{y} = f(\mathbf{x}; \mathbf{W}, \mathbf{b}) \quad (5)$$

where \mathbf{W} and \mathbf{b} denote the weights and bias, respectively. f denotes an activation function. The decoder is used to learn a mapping from the hidden layer \mathbf{y} to the output layer \mathbf{x}'

$$\tilde{\mathbf{x}} = f(\mathbf{y}; \tilde{\mathbf{W}}, \tilde{\mathbf{b}}). \quad (6)$$

The AE aims to generate an output which approximates to the input, extracting the latent features of the input. Thus, the loss function is the root-mean-square error, and the parameters can be updated using the ADAM algorithm [29]

$$\mathcal{L} = \|\mathbf{x} - \tilde{\mathbf{x}}\|_2. \quad (7)$$

III. AUTO-AD: AN AUTONOMOUS HYPERSPECTRAL ANOMALY DETECTION NETWORK BASED ON FULLY CONVOLUTIONAL AUTOENCODER

In this article, an autonomous hyperspectral anomaly detection network (Auto-AD) is proposed, in which the background is reconstructed by the network and the anomalies appear as reconstruction errors. A flowchart of the Auto-AD method is provided in Fig. 1. Specifically, through a fully convolutional AE with skip connections, the background can be reconstructed, whereas anomalies are difficult to reconstruct since the anomalies are relatively small compared to the background and only occur in the image with a low probability. Thus, the large reconstruction errors indicate potential anomalous pixels. However, an issue remains, in that the anomalies still have a low probability of being reconstructed during training. To further suppress the anomaly reconstruction, an adaptive-weighted loss function is designed, in which the weights of potential anomalous pixels are reduced during the training of the network. Accordingly, anomalies have a higher contrast with the background in the map of reconstruction errors.

TABLE I
NOTATION USED IN THIS ARTICLE

$\mathbf{X} \in \mathbb{R}^{H \times W \times B}$	Hyperspectral image with H rows, W columns, and B spectral bands
$\tilde{\mathbf{X}} \in \mathbb{R}^{H \times W \times B}$	Reconstructed background image with H rows, W columns, and B spectral bands
$d_{i,j}$	Reconstruction error at location (i, j)
$\mathbf{D} \in \mathbb{R}^{H \times W}$	Map of the reconstruction error
$w_{i,j}$	Weight at location (i, j)
$\mathbf{W} \in \mathbb{R}^{H \times W}$	Weight map

The proposed Auto-AD method is made up of two main parts, which are fully described in this section: 1) background reconstruction via the fully convolutional AE with skip connections; and 2) the adaptive-weighted loss function to suppress anomaly reconstruction. The autonomous property and **interpretability** of the Auto-AD method are also discussed. To better explain the proposed method, a summary of the notation is provided in Table I.

A. Fully Convolutional Autoencoder With Skip Connections to Reconstruct the Background

Given a hyperspectral image, the remaining parts should be anomalies after the background is separated, as long as the estimated background is accurate. Thus, the accuracy of the background estimation directly influences the accuracy of the anomaly detection. In the proposed network, the background is reconstructed via a fully convolutional AE with skip connections. The proposed network is essentially an unsupervised AE architecture. It is meant by “fully convolutional” that the network only involves convolutional layers, in addition to the batch normalization, activation, and upsampling functions, so as to generate the reconstruction for each pixel of the image. The main difference between a fully convolutional AE and a convolutional neural network is that the proposed network involves no fully connected layers or pooling layers. Since the network aims to reconstruct each pixel vector in the hyperspectral image, it is not necessary to assign labels to the pixels. In this case, a discriminative model is not involved in the proposed network, which is the main difference with a generative adversarial network (GAN). The network can learn the hierarchical, abstract, and high-level representations of the background from the hyperspectral data. As an unsupervised framework, it is applicable to the hyperspectral anomaly detection task.

The network architecture is composed of an encoder and a decoder, as shown in Fig. 1. To simplify the flowchart, seven blocks are used to represent the network architecture, with each block containing a convolutional layer.

1) *Encoder*: The encoder contains 15 convolutional layers, with each convolutional layer followed by batch normalization [36] and a Leaky rectified linear unit (LeakyReLU) activation function. Block #1 and block #4 each contain a 1×1 convolutional layer with a stride of 1. The feature maps

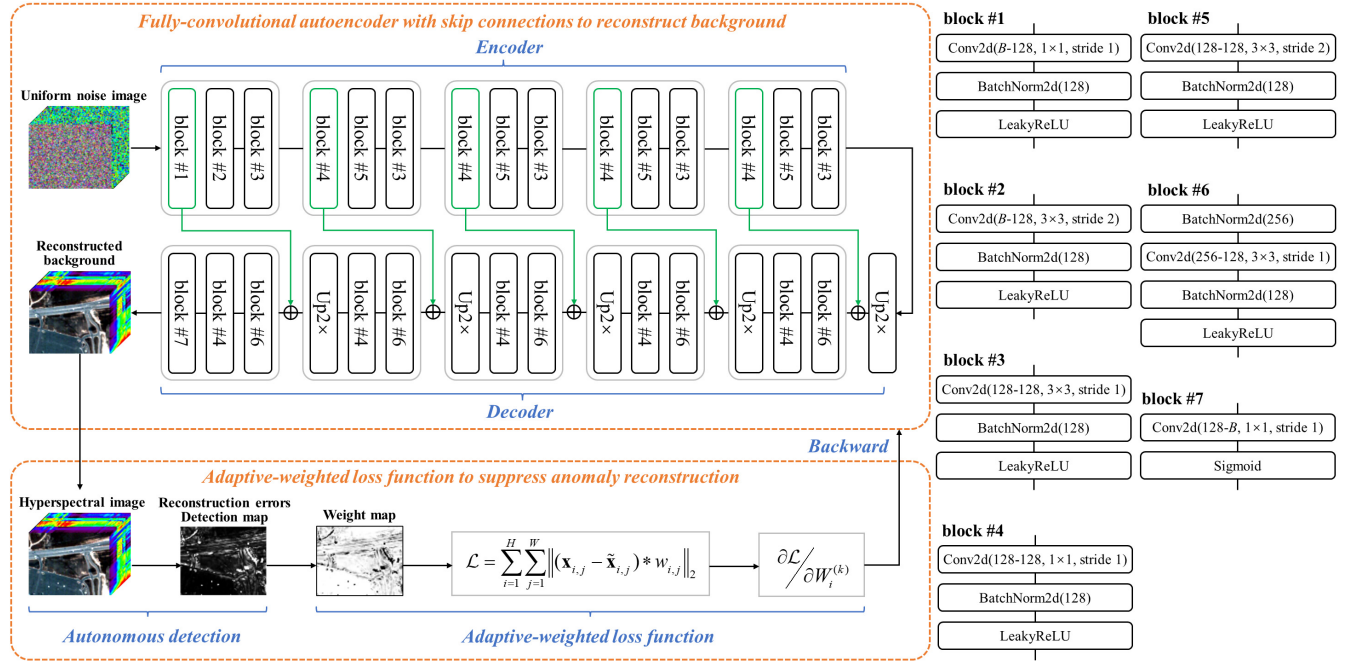


Fig. 1. Autonomous hyperspectral anomaly detection network based on fully convolutional autoencoder.

generated by block #1 and block #4 are not input into the next convolutional layer, but are concatenated with the feature maps of the corresponding layers of the decoder through skip connections, as denoted by the green lines in Fig. 1. During the decoding, the skip connections complement the features with spatial details in the earlier layers of the network [37], thus improving the spatial accuracy of the reconstructed background. In the encoder, except for the convolutional layer in block #2, which decreases the dimensionality of the hyperspectral image and generates a 128-dimension feature map, the other convolutional layers do not decrease the dimensionality of the feature map. This means that the dimensionality of the feature map remains unchanged at 128 during the encoding process. In this way, the spectral features are preserved. Note that the network aims to reconstruct the background, so that the features of the anomalies should be suppressed. The anomalies in hyperspectral imagery are usually small in size, and the number of anomalous pixels is very limited. Thus, the convolutional layers in block #2 and block #5 perform spatial downsampling, using a 3×3 convolutional layer with a stride of 2. The features of the anomalies are thus weakened in the feature maps during the encoding process. Block #3, which contains a 3×3 convolutional layer with a stride of 1, follows each block #2 and each block #5.

2) Decoder: The decoder contains 11 convolutional layers. Unlike the encoder, the decoder performs upsampling using nearest-neighbor interpolation with the scale of 2, as indicated in Fig. 1. The input of each block #6 is a 256-dimension feature map, i.e., the two 128-dimension feature maps are concatenated via the skip connections. Thus, in block #6, a 3×3 convolutional layer follows the batch normalization, and the input 256-dimension feature map is decreased to a 128-dimension feature map. Block #4, which contains

a 1×1 convolutional layer with a stride of 1, follows each block #6. The last block, block #7, contains a 1×1 convolutional layer with a stride of 1, through which the 128-dimension feature map is increased to the same dimensions as the original hyperspectral image. Unlike the other blocks, the convolutional layer in block #7 is followed by a sigmoid activation function.

The input of the network is an image filled with uniform noise, which has the same dimensionality as the input hyperspectral image, i.e., $\mathbf{X}^0 \in \mathbb{R}^{H \times W \times B}$. The values of the input image with uniform noise are all sampled from a uniform distribution in the range [0, 0.1]. The final output of the network is an image of a shape equal to the shape of the input hyperspectral image, which is referred to as the reconstructed background image.

B. Adaptive-Weighted Loss Function to Suppress Anomaly Reconstruction

With the training of the fully convolutional AE, the reconstruction error of the background is decreased. When the training process is complete, the map of reconstruction errors, which is composed of the reconstruction errors of all the image pixels, can be directly utilized for the anomaly detection. Although the reconstruction errors of the fully convolutional AE indicate the potential anomalies, the anomalies still have a low probability of being reconstructed. For the unweighted fully convolutional AE, as shown in Fig. 2(b), the background has been reconstructed, to some extent, while the anomalies have not been reconstructed after 300 iterations. When the training reaches 500 iterations, as shown in Fig. 2(c), the anomalies show a tendency to be reconstructed. The basic AE architecture is used to reconstruct the input

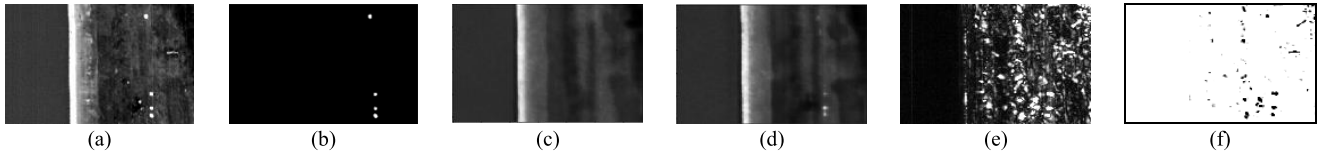


Fig. 2. Illustration of the motivation for the adaptive-weighted loss function. (a) Hyperspectral image. (b) Ground-truth map. (c) Iterations = 300 without weighting. (d) Iterations = 500 without weighting. (e) Map of reconstruction errors. (d) Weight map.

hyperspectral image. The background is dominant in the image and the anomalies occur with a low probability. Therefore, it is easier for the AE to reconstruct the background than the anomalies, which explains Fig. 2(b). As the training progresses, the network fits the data to a higher degree, and then the anomalies tend to be reconstructed, which explains Fig. 2(c). Therefore, the main issue is how to preserve the characteristics of the background while suppressing the reconstruction of the anomalies during the training. In this way, the map of reconstruction errors can be directly utilized for accurate anomaly detection, thus avoiding the need to construct an additional detector.

In this study, an adaptive-weighted loss function was designed for the proposed network. The reconstruction errors are fed backward to calculate a weighted loss, which is then fed backward for training. It is assumed that the anomalies have large reconstruction errors in the early stage of the training. Therefore, we reduce the weights of the regions with large reconstruction errors when calculating the loss in the early stage of the training. In this way, the reconstruction of anomalies is suppressed, realizing anomaly-free background reconstruction. The reconstruction error of each pixel can be calculated using the following:

$$e_{i,j} = \|\mathbf{x}_{i,j} - \tilde{\mathbf{x}}_{i,j}\|_2 \quad (8)$$

where $\mathbf{x}_{i,j}$ denotes the pixel vector of the input hyperspectral image, and $\tilde{\mathbf{x}}_{i,j}$ denotes the reconstructed pixel vector by the network. The map of reconstruction errors \mathbf{E} can then be obtained by combining the reconstruction errors of all the pixels

$$\mathbf{E} = [d_{1,1}, \dots, d_{1,W}; \dots; d_{H,1}, \dots, d_{H,W}] \quad (9)$$

The map of reconstruction errors is transformed into a weight map \mathbf{W} using the following:

$$w_{i,j} = \max(\mathbf{E}) - d_{i,j} \quad (10)$$

$$\mathbf{W} = [w_{1,1}, \dots, w_{1,W}; \dots; w_{H,1}, \dots, w_{H,W}] \quad (11)$$

where the small weights indicate the potential anomalous pixels, as shown in Fig. 2(f). This weight map is updated every 100 iterations. The elements of the weight map are all initialized as 1 in the first 100 iterations. The weight map reduces the contribution of anomalous pixels to the total loss. In this way, the anomalies avoid being reconstructed by the network as the training process goes on. Based on the weight map, the proposed adaptive-weighted loss can be calculated using the following:

$$\mathcal{L} = \sum_{i=1}^H \sum_{j=1}^W \|(\mathbf{x}_{i,j} - \tilde{\mathbf{x}}_{i,j})w_{i,j}\|_2 \quad (12)$$

Algorithm 1 Auto-AD

Input: hyperspectral image $\mathbf{X} \in \mathbb{R}^{H \times W \times B}$

Initialization: uniform noise image $\mathbf{X}^0 \in \mathbb{R}^{H \times W \times B}$, weight map $\mathbf{W}^0 \in \mathbb{R}^{H \times W}$

Training of the network:

Do ADAM until (13) is satisfied:

- 1: network forward;
- 2: update the weight map using (8)–(11) every 100 iterations;
- 3: calculate the adaptive-weighted loss using (12);
- 4: network backward.

End

Output: obtain the anomaly detection result using (14)–(15)

where $\mathbf{x}_{i,j} \in \mathbb{R}^{B \times 1}$ is the pixel vector at location (i, j) of the input hyperspectral image, $\tilde{\mathbf{x}}_{i,j} \in \mathbb{R}^{B \times 1}$ is the pixel vector at location (i, j) of the background image reconstructed by the network, and $w_{i,j}$ is the weight at location (i, j) .

The network is updated in an iterative training process to reconstruct the background. As shown in Fig. 1, in every iteration of the training, the network generates a reconstructed background with the input of a uniform noise image. The adaptive-weighted loss is then calculated. The loss is then fed backward to update the parameters of the network, for which the ADAM algorithm [38] is utilized. In the next iteration of the training, the above steps are repeated. The training stops when the average variation of the loss is below $\sigma = 1.5 \times 10^{-5}$ within the last 50 iterations:

$$\frac{1}{50} \sum_{i=k}^{k+50} (L^{i+1} - L^i) < \sigma \quad (13)$$

where k denotes the number of iterations.

After the iterative training process is completed, we obtain a trained network, denoted by $f_{\theta}(\cdot)$. The reconstructed background image $\mathbf{X}^b \in \mathbb{R}^{H \times W \times B}$ can be obtained through the trained network $f_{\theta}(\cdot)$ with the input of the uniform noise image using (14). Therefore, the final anomaly detection result can be obtained using (15), i.e., the reconstruction errors, where $\mathbf{x}_{i,j}^b$ is the pixel vector at location (i, j) of \mathbf{X}^b . In contrast, the existing AE-based methods need to construct an additional detector to realize anomaly detection

$$\mathbf{X}^b = f_{\theta}(\mathbf{X}^0) \quad (14)$$

$$D = \|\mathbf{x}_{i,j}^b - \tilde{\mathbf{x}}_{i,j}^b\|_2. \quad (15)$$

The proposed Auto-AD method is described in detail in Algorithm 1.

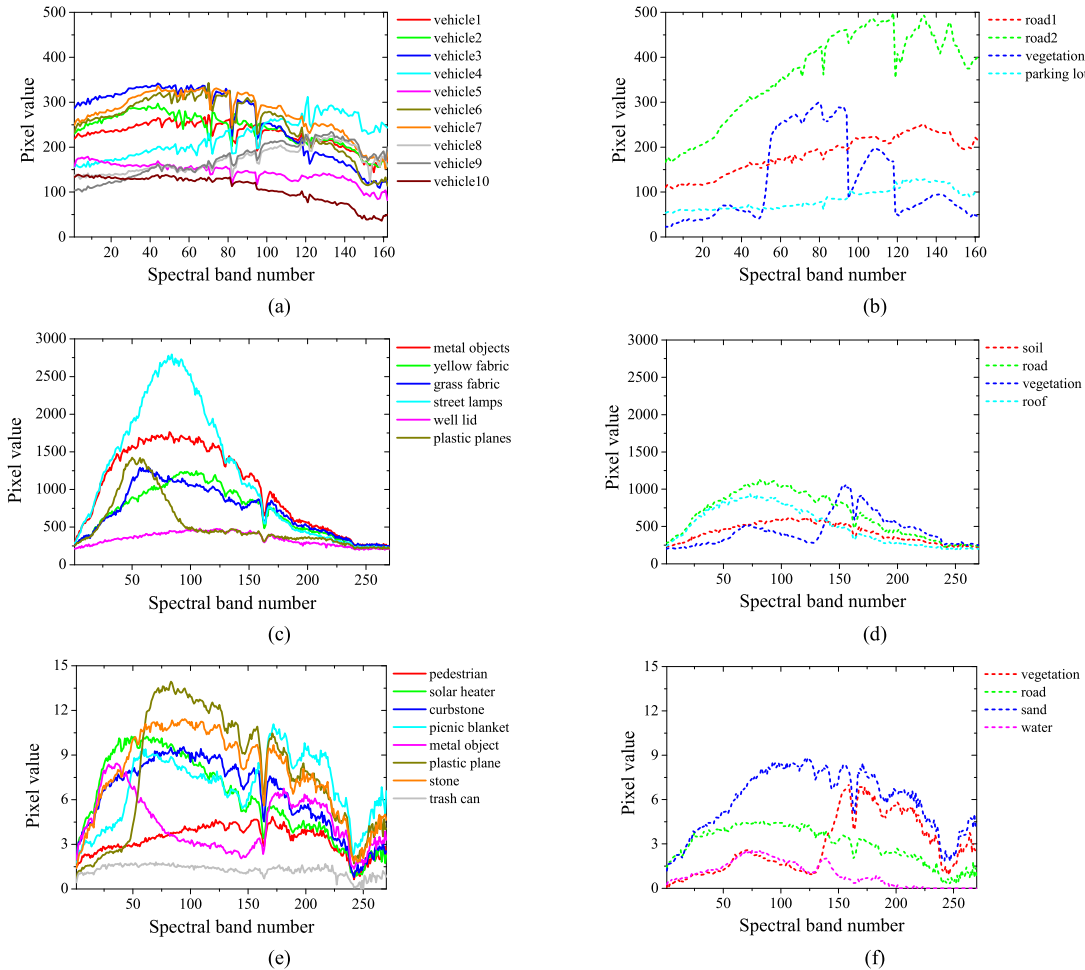


Fig. 3. Spectra of the anomalies and background of the experimental data sets. HYDICE dataset: (a) spectra of the anomalies; (b) spectra of the background. WHU-Hi-Station dataset: (c) spectra of the anomalies; (d) spectra of the background. WHU-Hi-Park dataset: (e) spectra of the anomalies; (f) spectra of the background.

IV. EXPERIMENTS AND ANALYSES

The proposed Auto-AD method was tested on a public airborne hyperspectral data set and two large unmanned aerial vehicle (UAV)-borne hyperspectral data sets and was compared with the classical global RX detector (GRX) [10], the anomaly detection method based on LRASR [19], the abundance- and dictionary-based low-rank decomposition (ADLR) method [20], and the unweighted fully convolutional AE with skip connections (UAE). The UAE method was used in the ablation experiments to verify the effectiveness of the proposed adaptive-weighted loss function. The experimental results are analyzed from both the qualitative and quantitative aspects.

A. Experimental Settings

1) *Data Set Description:* The first data set was collected by the Hyperspectral Digital Imagery Collection Experiment (HYDICE) sensor [39] over a suburban residential area of Michigan, USA. The spectral range of this data set is 400–2500 nm. The spatial resolution is 3 m per pixel. The image scene is of 80 × 100 pixels. A total of 162 spectral bands were retained after removing the bands of the water

absorption regions, low signal-to-noise ratio, and poor quality (1–4, 76, 87, 101–111, 136–153, and 198–210). The spectra of the anomalies and background materials are given in Fig. 3(a) and (b). In total, ten man-made vehicles are considered as the anomalies, with a total number of 17 pixels, and the background land-cover types are vegetation, soil, water, and road, as shown in Fig. 4(a) and (b).

Two UAV-borne hyperspectral data sets were also used in this study. The high spatial resolution of UAV-borne images provides abundant spatial information, which is useful for the fine recognition of materials. Owing to the high spatial resolution, UAV-borne hyperspectral remote sensing systems provide us with an efficient way to generate true hyperspectral data sets with ground-truth maps for quantitative assessment. In addition, the flexibility and low cost of the UAV platforms make it possible to conduct regular inspections and to respond quickly after a disaster [40], such as forest fire emergency response [41] and pest and disease monitoring in agriculture [42]. Anomaly detection in UAV-borne hyperspectral images shows great potential in such applications.

The first UAV-borne data set—the Wuhan University UAV-borne hyperspectral image (WHU-Hi) station data set

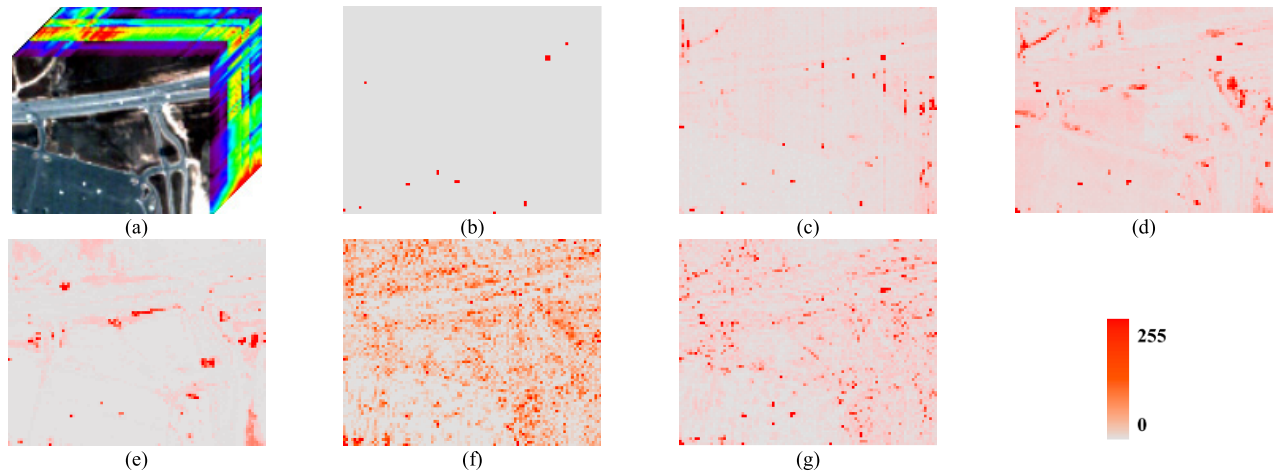


Fig. 4. HYDICE data set and the anomaly detection results. (a) RGB pseudo-color image. (b) Ground-truth map. (c) GRX. (d) LRASR. (e) ADLR. (f) UAE. (g) Auto-AD.

(the WHU-Hi-Station data set)—was collected by the Intelligent Data Extraction, Analysis and Application of Remote Sensing (RSIDEA) group of Wuhan University. This data set was obtained by a Nano-Hyperspec visible and near-infrared hyperspectral sensor mounted on a DJI M600 six-rotor UAV platform [40], [43]. The data collection was carried out on January 17, 2019, over a Satellite Earth Station in Wuhan, Hubei province of China. The flight height was 50 m, so that the spatial resolution of the acquired imagery is 4 cm per pixel. The image scene is of 4000×600 pixels in size, which is much larger than the commonly used hyperspectral anomaly detection data sets. The image has 270 bands and the spectral range is 400–1000 nm. The number of anomalous pixels is 1122, with a 0.047% proportion to the entire image. As the total data volume is large, this data set was split into $60\,200 \times 200$ blocks for the experiments.

The third data set—the Wuhan University UAV-borne hyperspectral image (WHU-Hi) park data set (WHU-Hi-Park data set)—was also collected by the RSIDEA group with the same mini-UAV-borne hyperspectral remote sensing system as that of the WHU-Hi-Station data set. The experimental area is Zhengzhou, Henan province, China. The data collection was carried out on March 27, 2019, over a city park. The flight height of the UAV was 100 m, so that the spatial resolution of the acquired imagery is 8 cm per pixel. The image contains 600×2000 pixels and 270 spectral bands in the 400–1000 nm spectral range. This data set is also much larger than the commonly used hyperspectral anomaly detection data sets. The number of anomalous pixels is 1510, with a 0.126% proportion to the entire image. The WHU-Hi-Park data set was also split into 200×200 blocks for the experiments.

A field survey was also conducted during the data collection to determine the classes of the anomalies. The class information was only used to describe the data sets, and was not used in the anomaly detection experiments. Four features have been suggested to characterize anomalies [44]: 1) no prior knowledge of existence; 2) low probability of occurrence; 3) insignificance in spectral statistics; and 4) small size of population. The anomalies in the two experimental UAV-borne

TABLE II
DESCRIPTION OF THE ANOMALIES IN THE WHU-HI STATION DATA SET

Anomaly		Description	Pixels	Ratio
M1, M2, M3, M4 M5, M6, M7, M8		Metal objects	387	0.0158%
C	C1, C2	Objects covered with yellow fabric	199	0.0083%
	C3, C4	Objects covered with green fabric		
L1, L2, L3		Streetlamps	160	0.0067%
W1		Well lid	112	0.0047%
P1, P2, P3		Plastic plates	264	0.011%

TABLE III
DESCRIPTION OF THE ANOMALIES IN THE WHU-HI-PARK DATA SET

Anomaly		Description	Pixels	Ratio
SC1, SC2, SC3, SC4		Stone columns	122	0.01%
T1		Trash can	40	0.0033%
P1, P2		Plastic planes	244	0.02%
S1		Stone	21	0.0018%
M1		Metal object	176	0.015%
B1		Picnic blanket	552	0.046%
K1, K2, K3, K4		Curbstones	242	0.02%
H1		Solar heater	40	0.0033%
PP		Pedestrian	73	0.0061%

hyperspectral data sets were characterized based on these four features (see Tables II and III). No prior knowledge is available about the anomalies, so feature 1) is satisfied. Feature 2) and feature 3) can be reflected via the proportion of anomalous pixels to the total number of image pixels. As shown in Tables II and III, the proportion of every anomaly is very low, and thus the anomalies defined in the data sets satisfy feature 2) and feature 3). C.-I. Chang gave a threshold to define the size of an anomaly. i.e., $n = [N/100]$, where N is the total number of pixels in the image [44]. In this case, the thresholds would be defined as 24 000 and 12 000 for the WHU-Hi-Park data set and the WHU-Hi-Station data set, respectively. However, anomalies which have more than

10 000 pixels are visually obvious. Therefore, the threshold should be defined as at least $n = \lceil N/1000 \rceil$ for UAV-borne hyperspectral data sets, i.e., 2400 and 1200 for the WHU-Hi-Park data set and the WHU-Hi-Station data set, respectively. As shown in Tables II and III, the anomalies defined in these two UAV-borne hyperspectral data sets are all smaller than the threshold, and thus feature 4) is satisfied.

2) *Parameter Settings*: For the GRX method, a covariance matrix is first calculated based on the entire image, which is then input into each block to calculate the Mahalanobis distance of each pixel. According to the description in the original article of LRASR, the number of clusters K and the number of selected pixels P were set to 15 and 20, respectively, and the regularization parameters β and λ were set to 0.1 for all three experimental data sets. The ADLR method has three free parameters: the number of endmembers c , the bandwidth in the mean-shift algorithm bw , and the regularization parameter λ , which were, respectively, set to 21, 0.21, and 0.02 for the HYDICE data set and 15, 0.2, and 0.02 for the WHU-Hi-Station data set and WHU-Hi-Park data set.

B. Experimental Results

In this part, the detection results of the proposed Auto-AD method and those of the other methods are qualitatively analyzed. The 2-D plots for the obtained detection results are provided in Figs. 4–6, in which all the detection maps are linearly stretched to [0, 255] for display.

1) *Airborne HYDICE Data Set*: For the HYDICE data set, which is frequently used in hyperspectral anomaly detection research, as shown in Fig. 4, although there are fewer false alarms in the results of GRX than the results of Auto-AD, the anomalies in the results of the proposed method show stronger responses than those in the results of GRX. In fact, the responses of the false alarms in the results of Auto-AD are much weaker than the responses of the anomalies, and the false alarm rate is very low when achieving a 100% probability of detection. Compared with the results of the low-rank-based methods—LRASR and ADLR—there are no background regions with strong responses in the results of Auto-AD. Comparing Fig. 4(f) and (g), some anomalies in the results of UAE are not as obvious as those in the results of Auto-AD, which means that these anomalies tend to be reconstructed, but Auto-AD solves this problem, to a certain extent.

2) *UAV-Borne WHU-Hi-Station and WHU-Hi-Park Data Sets*: For the WHU-Hi-Station and WHU-Hi-Park data sets, which were used to test the performance of the methods on large hyperspectral images, as shown in Figs. 5 and 6, the overall response of the background is weaker in the result of the proposed Auto-AD method, while all the anomalies are also detected. However, in the detection results of LRASR, a “patch phenomenon” can be observed.

The different blocks vary in spectral and spatial characteristics, and also have different data distributions, but the same parameter setting of LRASR cannot adapt to all the blocks. Therefore, for the LRASR method, the detection performance varies between the different blocks on the UAV-borne hyperspectral data sets, which explains the “patch phenomenon.”

In addition, it is difficult in practical application to adjust the parameters for different data sets. As an autonomous anomaly detection network, the proposed Auto-AD method requires no manual parameter setting. Furthermore, the proposed method achieves a superior detection performance on all the blocks, with no seam lines in the detection results. Although GRX also has no free parameters, the response of the background is much stronger than for the proposed Auto-AD method. On both data sets background regions with strong responses exist (the red regions in the detection maps) in the results of GRX and LRASR, while these background regions are better suppressed in the results of the proposed Auto-AD method. Although the results of ADLR contain less noise than the results of GRX and LRASR, the anomalies (such as C2 and M8) are not obvious visually. In the results of UAE with the WHU-Hi-Station data set, some anomalies (such as C1 and W1) in the upper half of the image show weak responses, and have the tendency to be reconstructed. In addition, in the results of UAE on the WHU-Hi-Park data set, the picnic blanket (B1) in the middle of the image exhibits a weak response. In contrast, the anomalies present stronger responses in the results of Auto-AD, which means that these anomalies are blocked from being reconstructed, owing to the proposed adaptive-weighted loss function.

C. Quantitative Evaluation

In this part, the detection results are analyzed quantitatively. To this aim, multiparameter receiver operating characteristic (3-D ROC) curves [44], [45], the area under the curve (AUC) [46], and separability maps [19] are employed.

Conventional 2-D ROC curves [47], which are plotted by the probability of detection (P_D) and false alarm rate (P_F), are an effective way to assess the effectiveness of a hyperspectral anomaly detection method. Actually, P_D and P_F are dependent parameters resulting from the threshold τ , whereas 2-D ROC curves cannot convey the information of the threshold τ . In this article, 3-D ROC curves are employed to assess the effectiveness of the experimental methods. 3-D ROC curves are plotted by three parameters: P_D , P_F , and τ . The detection map should be normalized in the range of [0, 1], and the pairs of P_D and P_F can be calculated when τ is varied from 1 to 0. The 3-D ROC curve can then be plotted by (P_D, P_F, τ) . Three 2-D ROC curves can be derived from the 3-D ROC curve: the conventional 2-D ROC curve (P_D, P_F) and two new 2-D ROC curves plotted by (P_D, τ) and (P_F, τ) , respectively. The conjoint analysis of the curves of (P_D, τ) and (P_F, τ) can help to determine whether a method can achieve detection with simultaneous high P_D and low P_F . Furthermore, a proper threshold range can be determined for the subsequent binary decision. An effective method should have a larger area under the 2-D ROC curve of (P_D, P_F) , and a smaller area under the 2-D ROC curve of (P_D, τ) and (P_F, τ) . The 3-D ROC curves are displayed in Fig. 7. The AUC scores of the conventional 2-D ROC curves (P_D, P_F) and the time consumption are listed in Table IV, where the figures in bold are the best results and the underlined figures are the second-best results.

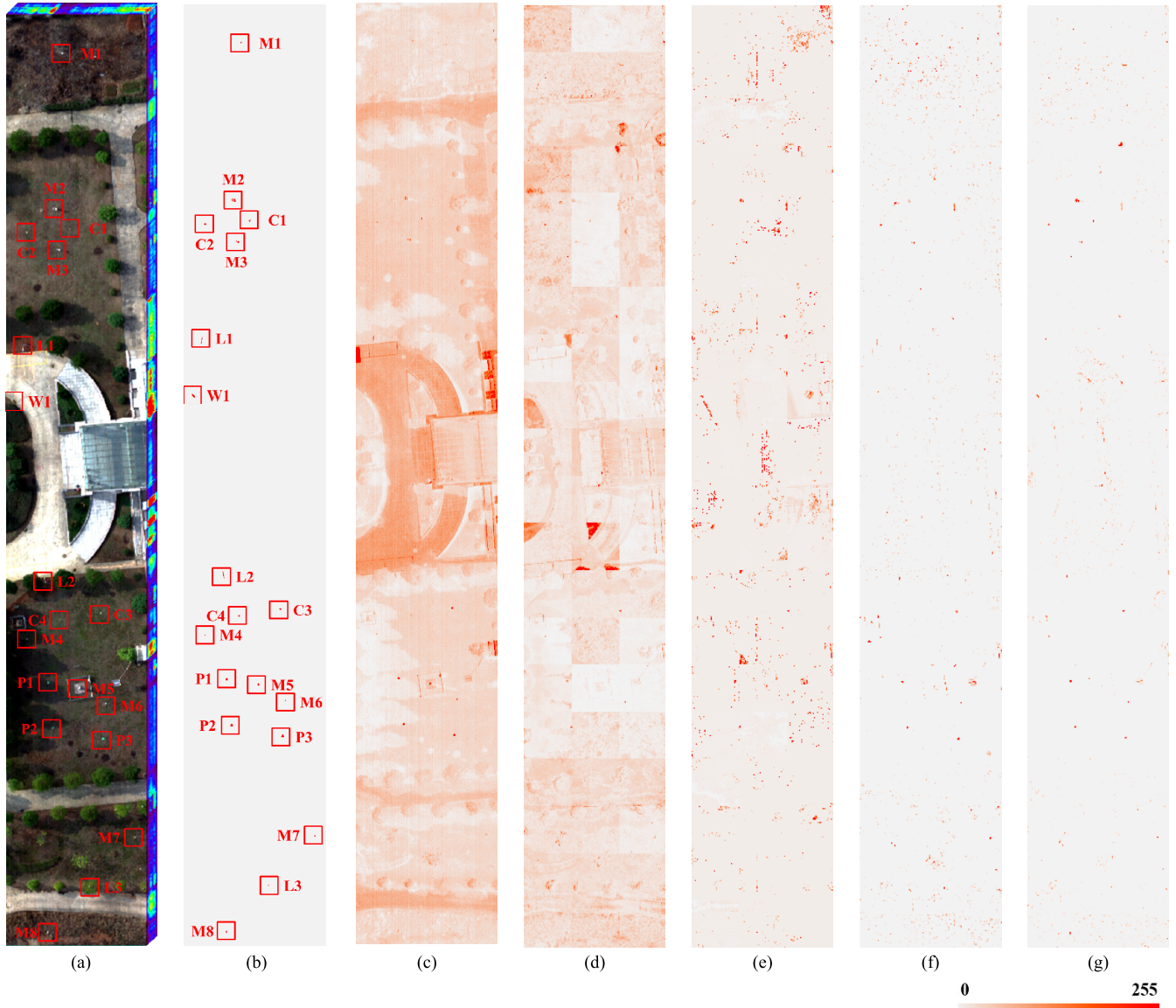


Fig. 5. WHU-Hi-Station data set and the anomaly detection results. (a) RGB pseudo-color image. (b) Ground-truth map. (c) GRX. (d) LRASR. (e) ADLR. (f) UAE. (g) Auto-AD.

TABLE IV
AUC SCORES OF THE 2-D ROC CURVES AND
TIME CONSUMPTION (SECONDS)

		GRX	LRASR	ADLR	UAE	Auto-AD
HYDICE	AUC	0.9938	0.9920	0.9624	0.9721	0.9991
	Time	0.14	23.48	49.32	75.90	67.81
WHU-Hi-Station	AUC	0.9004	0.8323	0.9094	<u>0.9550</u>	0.9852
	Time	99	11428	19238	5208	4570
WHU-Hi-Park	AUC	0.9178	0.8529	0.6045	<u>0.9262</u>	0.9830
	Time	36	4928	12255	3252	2896

Separability maps are also employed to assess the background suppression of the methods. The detection maps should be normalized in the range of [0, 1], and then the distributions of the anomalous pixels' values and the background

pixels' values can be compared via the box charts. As shown in Fig. 11, the green box denotes the anomalous pixels' values in the range of [10%, 90%], and the red box denotes the background. The lines at the top and bottom of each box stand for the extreme values, and the median line denotes the mid-value of the pixels' values. The background is effectively suppressed when the width of the background box is short and the anomaly box is separated from the background box.

1) HYDICE Data Set: For the HYDICE data set, as shown in Fig. 8(a), the 2-D ROC curve (P_D , P_F) of Auto-AD is above those of the competing methods. Auto-AD, UAE, GRX, LRASR, and ADLR have P_F values of approximately 0.8%, 8.97%, 2%, 17%, and 24%, respectively, when achieving a 100% P_D . In addition, the false alarm rate for Auto-AD is much lower than that for UAE, which means that the anomalies are further separated from the background. The proposed method also achieves the highest AUC score of 0.9996.

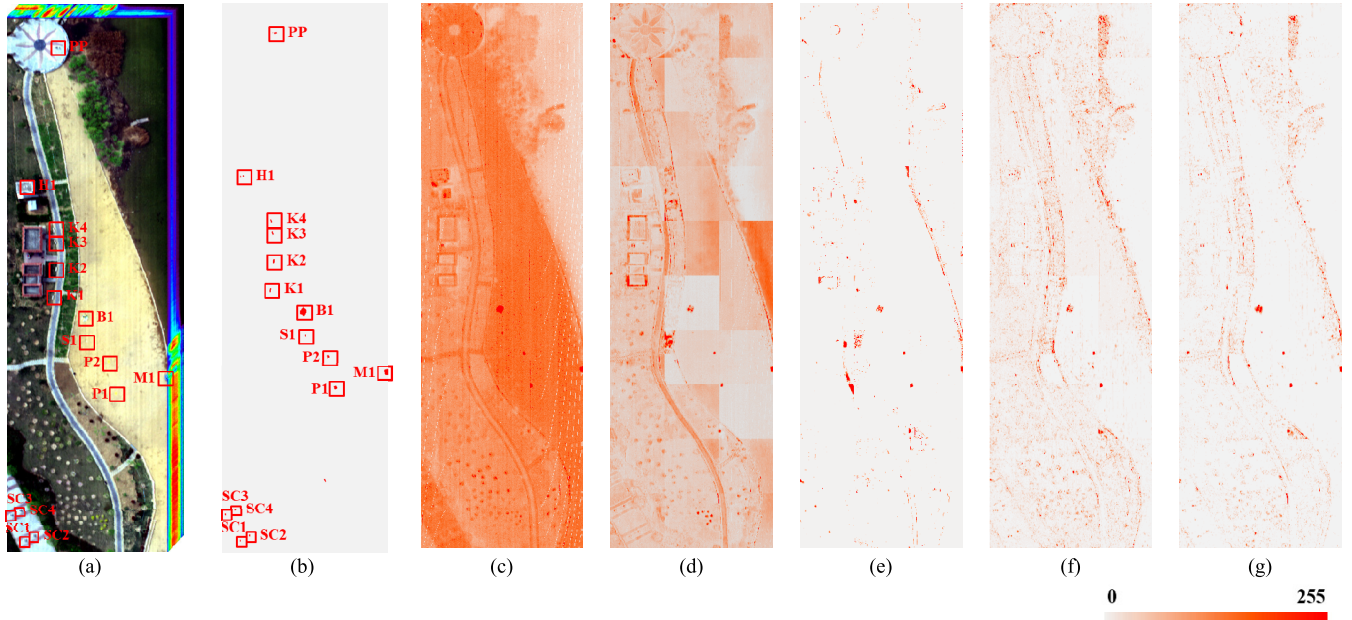


Fig. 6. WHU-Hi-Park data set and the anomaly detection results. (a) RGB pseudo-color image. (b) Ground-truth map. (c) GRX. (d) LRASR. (e) ADLR. (f) UAE. (g) Auto-AD.

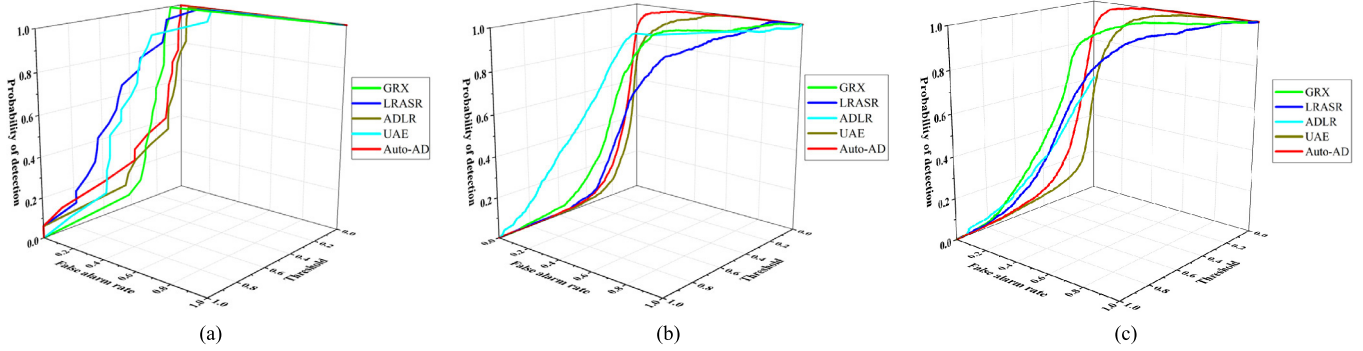


Fig. 7. 3-D ROC curves. (a) HYDICE data set. (b) WHU-Hi-Station data set. (c) WHU-Hi-Park data set.

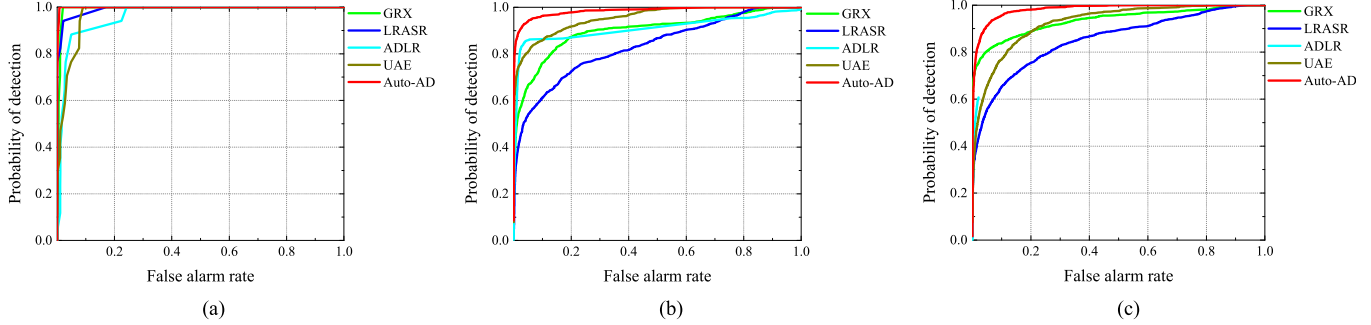


Fig. 8. 2-D ROC curves (P_D , P_F). (a) HYDICE data set. (b) WHU-Hi-Station data set. (c) WHU-Hi-Park data set.

The 2-D ROC curves of (P_D, τ) and (P_F, τ) are shown in Figs. 9(a) and 10(a), where Auto-AD, LRASR, and GRX achieve P_D values of more than 90% when P_F is very close to 0. Taking all these results together, Auto-AD shows its superiority in most of these indices. A possible threshold τ for Auto-AD is 0.01364, where P_D is 100% and P_F is 0.79%. The separability maps for the HYDICE data set are

shown in Fig. 11(a). The anomaly box and background box are separated for all the methods, except for ADLR. The background box for Auto-AD has the shortest width, which means that the background is effectively suppressed in the detection result of Auto-AD.

2) *WHU-Hi-Station Data Set*: For the WHU-Hi-Station data set, the proposed Auto-AD method achieves a significant

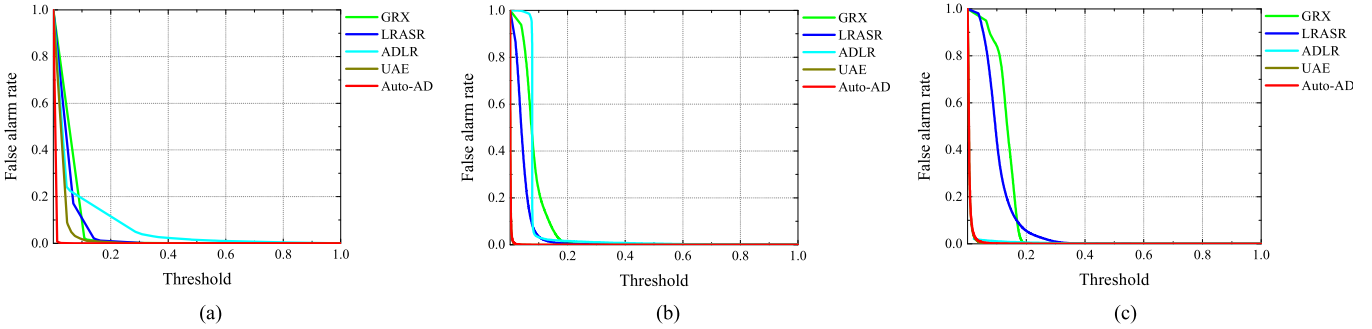
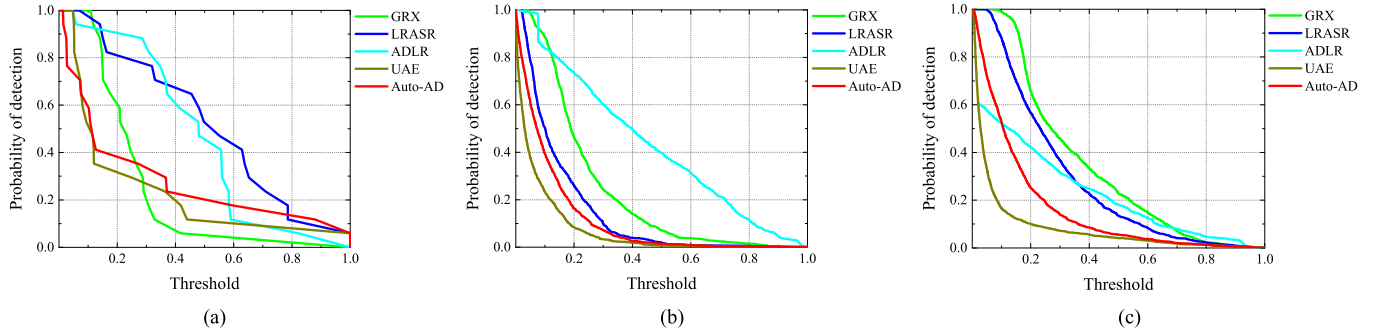
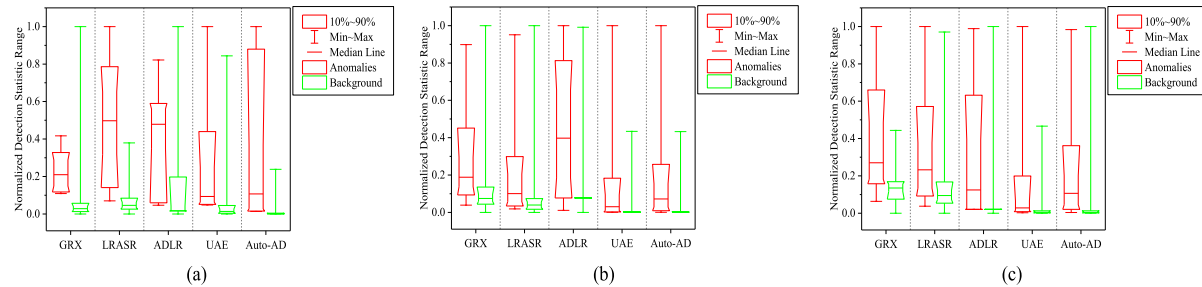
Fig. 9. 2-D ROC curves (P_F, τ). (a) HYDICE data set. (b) WHU-Hi-Station data set. (c) WHU-Hi-Park data set.Fig. 10. 2-D ROC curves (P_D, τ). (a) HYDICE data set. (b) WHU-Hi-Station data set. (c) WHU-Hi-Park data set.

Fig. 11. Separability maps. (a) HYDICE data set. (b) WHU-Hi-Station data set. (c) WHU-Hi-Park data set.

increase in detection accuracy. Where the other methods can only obtain an AUC score of around or below 0.9, Auto-AD achieves a much higher AUC score of 0.9852. The 2-D ROC curves (P_D, P_F) are shown in Fig. 8(b), where the curve of the Auto-AD method is separate from those of the other methods. When achieving a 100% P_D , the P_F of Auto-AD, UAE, GRX, LRASR, and ADLR is approximately 76%, 67%, 94%, 87%, and 100%, respectively. When comparing Auto-AD (30%) and UAE (27.9%), it can be seen that the adaptive-weighted loss function inhibits the tendency of anomalies to be reconstructed, to some extent. The 2-D ROC curves of (P_D, τ) and (P_F, τ) are shown in Figs. 9(b) and 10(b), where only Auto-AD can achieve a P_D value of beyond 80% when P_F is very close to 0. A possible threshold τ is 0.01227, where P_D is 86.54% and P_F is 1%. The separability maps for the WHU-Hi-Station data set are displayed in Fig. 11(b), where the background boxes are not separated from the anomaly boxes, except for the proposed Auto-AD method.

3) *WHU-Hi-Park Data Set*: For the WHU-Hi-Park data set, the anomalies vary in spatial size, which increases the difficulty of the detection. The proposed Auto-AD method obtains the highest AUC score of 0.9830, which is much higher than the competing methods. As shown in Fig. 8(c), the 2-D ROC curve (P_D, P_F) of Auto-AD is always above the curves of GRX, LRASR, ADLR, and UAE. In the results of ADLR, some anomalies are not detected, and the curve does not reach 100% P_D , which explains why the AUC score of ADLR on this data set is only 0.6045. When achieving a 100% probability of detection, the false alarm rates of Auto-AD, UAE, GRX, and LRASR are approximately 64.18%, 88.47%, 95%, and 98.1%, respectively, in which the P_F of Auto-AD is much lower than that of UAE, demonstrating that the anomaly reconstruction is suppressed. The 2-D ROC curves of (P_D, τ) and (P_F, τ) are shown in Figs. 9(c) and 10(c), where only Auto-AD can achieve a P_D value beyond 80% when P_F is very close to 0. A possible threshold τ is 0.03673, where P_D is 80%

and P_F is 1.4%. In the separability maps for the WHU-Hi-Park data set, as shown in Fig. 11(c), ADLR does not detect all the anomalous pixels, although the background box is separated from the anomaly box. For GRX and LRASR, the background box is overlapped with the anomaly box. The background box is slightly more separated from the anomaly box for Auto-AD than UAE, and the gap between the background box and the median line of the anomaly box is also larger for Auto-AD than UAE.

For the UAV-borne WHU-Hi-Station and WHU-Hi-Park data sets, none of the methods achieve very high P_D values with small values of P_F . The reasons for this lie in two main aspects: 1) the background is quite complicated. The heterogeneity of the background is greatly enhanced in the two experimental UAV-borne data sets, in which the spatial resolution reaches 4 cm and 8 cm, respectively; 2) the total number of pixels is large while the proportion of anomalous pixels is quite low. These two factors greatly increase the difficulty of the anomaly detection, causing false alarms, but the proposed Auto-AD method achieves the highest accuracy on these two UAV-borne hyperspectral data sets.

The run times of the experimental methods are listed in Table IV. GRX requires less time; however, the detection accuracy of GRX is much lower than that of the proposed Auto-AD method on the two large UAV-borne hyperspectral data sets, i.e., the WHU-Hi-Station data set and the WHU-Hi-Park data set. Compared with the two low-rank-based methods—LRASR and ADLR—Auto-AD exhibits obvious time efficiency on the WHU-Hi-Station and WHU-Hi-Park data sets. Furthermore, UAE requires more time to reach convergence because anomalies are involved in the background reconstruction, and it is difficult to reconstruct the anomalies.

4) *Additional Public Data Sets*: To further test the performance of the proposed Auto-AD method, experiments on other several public data sets have been carried out. The public data sets are listed in Fig. 12. The Honghu data set [49] covers the spectral range of 400–1000 nm with 135 spectral bands. The image scene is of 105×168 pixels in size and the anomalies account for 2.04% of the image. The PHI data set [9] is simulated by embedding the anomaly spectrum andradite from the ENVI spectral library into certain pixels with a predetermined percentage. This data set covers the spectral range of 440 to 854 nm with 80 spectral bands and 240×240 pixels, in which the anomalies account for 0.17% of the image. The ROSIS data set [9] covers the spectral range of 430 to 860 nm with 102 spectral bands and 108×120 pixels, in which the anomalies account for 0.33% of the image. LRASR involves four parameters, including the number of clusters K , number of pixels chosen to form dictionary P , regularization parameters λ and β . For the Honghu and ROSIS data sets, the parameters are set as $K = 15$, $P = 20$, $\lambda = 0.1$, $\beta = 0.1$. The AUC score of PHI data set refers to that in [9]. ADLR involves three parameters, including the number of endmembers c , bandwidth in clustering bw , and regularization parameter λ . The parameters of ADLR are set as $c = 10$, $bw = 0.2$, $\lambda = 0.02$, $c = 20$, $bw = 0.3$, $\lambda = 0.03$

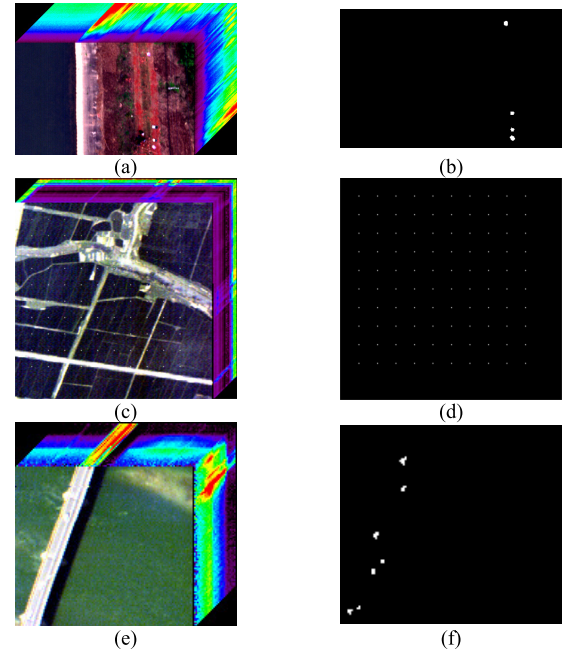


Fig. 12. Additional public data sets. Honghu data set: (a) RGB pseudo-color image. (b) Ground-truth map. PHI data set. (c) RGB pseudo-color image. (d) Ground-truth map. ROSIS data set. (e) RGB pseudo-color image. (f) Ground-truth map.

TABLE V
AUC SCORES OF ADDITIONAL PUBLIC DATA SETS

	GRX	LRASR	ADLR	UAE	Auto-AD
Honghu	0.9989	0.9879	0.9313	0.9931	<u>0.9974</u>
PHI	0.9281	0.9485 [9]	0.9338	<u>0.9774</u>	0.9806
ROSIS	<u>0.9983</u>	0.9801	0.9981	0.9905	0.9986

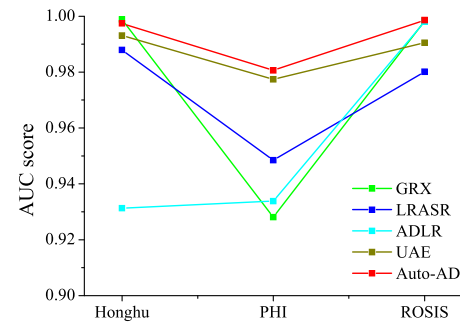


Fig. 13. Additional public data sets.

and $c = 20$, $bw = 0.3$, $\lambda = 0.02$ for the Honghu data set, PHI data set, and ROSIS data set, respectively.

The AUC scores are listed in Table V, where the proposed Auto-AD method achieves the highest AUC score on the PHI and ROSIS data sets, and the second-highest AUC score on the Honghu data set. Although GRX achieves a higher AUC score than Auto-AD on the Honghu data set, Auto-AD exhibits much higher detection accuracy on the PHI data set. Furthermore, the proposed Auto-AD method exhibits better robustness on these three public data sets, as shown in Fig. 13, the curve of Auto-AD exhibits the smallest variation of AUC scores on all the experimental data sets.

V. CONCLUSION

In this article, we have proposed an autonomous hyperspectral anomaly detection network based on fully convolutional AE (Auto-AD), in which the background is reconstructed by the network while the anomalies appear as reconstruction errors. Although large reconstruction errors in the network indicate the potential anomalies, the anomalies still have a low probability of being reconstructed during the training for the background estimation. To further suppress the anomaly reconstruction, an adaptive-weighted loss function is designed, in which the reconstruction errors are fed back to reduce the contribution of potential anomalous pixels with large reconstruction errors to the total loss. The experiments on an airborne data set and two large UAV-borne data sets demonstrated the effectiveness of the proposed Auto-AD algorithm.

In the future, saliency-based methods [48] will be investigated for the extraction of potential anomalies, to further maintain the characteristics of the anomalies in the map of reconstruction errors. In addition, the authors will investigate the potential applications of UAV-borne hyperspectral images [40]. Owing to the abundant spectral information, UAV-borne hyperspectral images exhibit advantages in detecting targets which are invisible in RGB images but show identifiable features in hyperspectral images.

VI. ACKNOWLEDGMENT

The authors would like to thank the Editor, Associate Editor, and Anonymous Reviewers for their helpful comments and suggestions to improve this article, and the authors of “*Deep Image Prior*,” “*Deep Hyperspectral Prior: Denoising, Inpainting, Super-Resolution*,” LRASR, and ADLR algorithms for sharing their codes. The authors would also like to give special thanks to the NBL Imaging System Ltd., for its assistance during the WHU-Hi-Station and WHU-Hi-Park dataset collection.

REFERENCES

- [1] A. F. H. Goetz, G. Vane, J. E. Solomon, and B. N. Rock, “Imaging spectrometry for earth remote sensing,” *Science*, vol. 228, no. 4704, pp. 1147–1153, Jun. 1985.
- [2] D. Landgrebe, “Hyperspectral image data analysis,” *IEEE Signal Process. Mag.*, vol. 19, no. 1, pp. 17–28, Jan. 2002.
- [3] L. Zhang, Q. Zhang, B. Du, X. Huang, Y. Y. Tang, and D. Tao, “Simultaneous spectral-spatial feature selection and extraction for hyperspectral images,” *IEEE Trans. Cybern.*, vol. 48, no. 1, pp. 16–28, Jan. 2018.
- [4] M. Zhang, W. Li, Q. Du, L. Gao, and B. Zhang, “Feature extraction for classification of hyperspectral and LiDAR data using patch-to-patch CNN,” *IEEE Trans. Cybern.*, vol. 50, no. 1, pp. 100–111, Jan. 2020.
- [5] D. W. J. Stein, S. G. Beaven, L. E. Hoff, E. M. Winter, A. P. Schaum, and A. D. Stocker, “Anomaly detection from hyperspectral imagery,” *IEEE Signal Process. Mag.*, vol. 19, no. 1, pp. 58–69, Jan. 2002.
- [6] Y. Yuan, D. Ma, and Q. Wang, “Hyperspectral anomaly detection by graph pixel selection,” *IEEE Trans. Cybern.*, vol. 46, no. 12, pp. 3123–3134, Dec. 2016.
- [7] D. G. Manolakis, “Taxonomy of detection algorithms for hyperspectral imaging applications,” *Opt. Eng.*, vol. 44, no. 6, pp. 1–11, Jun. 2005.
- [8] S. Matteoli, T. Veracini, M. Diani, and G. Corsini, “Models and methods for automated background density estimation in hyperspectral anomaly detection,” *IEEE Trans. Geosci. Remote Sens.*, vol. 51, no. 5, pp. 2837–2852, May 2013.
- [9] R. Zhao, B. Du, L. Zhang, and L. Zhang, “A robust background regression based score estimation algorithm for hyperspectral anomaly detection,” *ISPRS J. Photogramm. Remote Sens.*, vol. 122, pp. 126–144, Dec. 2016.
- [10] Z. Wu, W. Zhu, J. Chanussot, Y. Xu, and S. Osher, “Hyperspectral anomaly detection via global and local joint modeling of background,” *IEEE Trans. Signal Process.*, vol. 67, no. 14, pp. 3858–3869, Jul. 2019.
- [11] I. S. Reed and X. Yu, “Adaptive multiple-band CFAR detection of an optical pattern with unknown spectral distribution,” *IEEE Trans. Acoust., Speech, Signal Process.*, vol. 38, no. 10, pp. 1760–1770, Oct. 1990.
- [12] H. Kwon and N. M. Nasrabadi, “Kernel RX-algorithm: A nonlinear anomaly detector for hyperspectral imagery,” *IEEE Trans. Geosci. Remote Sens.*, vol. 43, no. 2, pp. 388–397, Feb. 2005.
- [13] Q. Guo, B. Zhang, Q. Ran, L. Gao, J. Li, and A. Plaza, “Weighted-RXD and linear filter-based RXD: Improving background statistics estimation for anomaly detection in hyperspectral imagery,” *IEEE J. Sel. Topics Appl. Earth Observ. Remote Sens.*, vol. 7, no. 6, pp. 2351–2366, Jun. 2014.
- [14] N. Billor, A. S. Hadi, and P. F. Velleman, “BACON: Blocked adaptive computationally efficient outlier nominators,” *Comput. Statist. Data Anal.*, vol. 34, no. 3, pp. 279–298, Sep. 2000.
- [15] B. Du and L. Zhang, “Random-selection-based anomaly detector for hyperspectral imagery,” *IEEE Trans. Geosci. Remote Sens.*, vol. 49, no. 5, pp. 1578–1589, May 2011.
- [16] N. Huyan, X. Zhang, H. Zhou, and L. Jiao, “Hyperspectral anomaly detection via background and potential anomaly dictionaries construction,” *IEEE Trans. Geosci. Remote Sens.*, vol. 57, no. 4, pp. 2263–2276, Apr. 2019.
- [17] J. Li, H. Zhang, L. Zhang, and L. Ma, “Hyperspectral anomaly detection by the use of background joint sparse representation,” *IEEE J. Sel. Topics Appl. Earth Observ. Remote Sens.*, vol. 8, no. 6, pp. 2523–2533, Jun. 2015.
- [18] W. Li and Q. Du, “Collaborative representation for hyperspectral anomaly detection,” *IEEE Trans. Geosci. Remote Sens.*, vol. 53, no. 3, pp. 1463–1474, Mar. 2015.
- [19] Y. Zhang, D. Bo, L. Zhang, and S. Wang, “A low-rank and sparse matrix decomposition-based Mahalanobis distance method for hyperspectral anomaly detection,” *IEEE Trans. Geosci. Remote Sens.*, vol. 54, no. 3, pp. 1376–1389, Mar. 2015.
- [20] Y. Xu, Z. Wu, J. Li, A. Plaza, and Z. Wei, “Anomaly detection in hyperspectral images based on low-rank and sparse representation,” *IEEE Trans. Geosci. Remote Sens.*, vol. 54, no. 4, pp. 1990–2000, Apr. 2016.
- [21] Y. Qu et al., “Hyperspectral anomaly detection through spectral unmixing and dictionary-based low-rank decomposition,” *IEEE Trans. Geosci. Remote Sens.*, vol. 56, no. 8, pp. 4391–4405, Aug. 2018.
- [22] Y. Xu, Z. Wu, J. Chanussot, and Z. Wei, “Joint reconstruction and anomaly detection from compressive hyperspectral images using mahalanobis distance-regularized tensor RPCA,” *IEEE Trans. Geosci. Remote Sens.*, vol. 56, no. 5, pp. 2919–2930, May 2018.
- [23] X. Zhou, C. Yang, and W. Yu, “Moving object detection by detecting contiguous outliers in the low-rank representation,” *IEEE Trans. Pattern Anal. Mach. Intell.*, vol. 35, no. 3, pp. 597–610, Mar. 2013.
- [24] N. P. Galatsanos and A. K. Katsaggelos, “Methods for choosing the regularization parameter and estimating the noise variance in image restoration and their relation,” *IEEE Trans. Image Process.*, vol. 1, no. 3, pp. 322–336, Jul. 1992.
- [25] O. Sidorov and J. Yingve Hardeberg, “Deep hyperspectral prior: Denoising, inpainting, super-resolution,” 2019, arXiv:1902.00301. [Online]. Available: <http://arxiv.org/abs/1902.00301>
- [26] V. Lempitsky, A. Vedaldi, and D. Ulyanov, “Deep image prior,” in *Proc. IEEE/CVF Conf. Comput. Vis. Pattern Recognit.*, Jun. 2018, pp. 9446–9454.
- [27] C. Zhao, X. Li, and H. Zhu, “Hyperspectral anomaly detection based on stacked denoising autoencoders,” *J. Appl. Remote Sens.*, vol. 11, no. 4, p. 1, Sep. 2017.
- [28] C. Zhao and L. Zhang, “Spectral-spatial stacked autoencoders based on low-rank and sparse matrix decomposition for hyperspectral anomaly detection,” *Infr. Phys. Technol.*, vol. 92, pp. 166–176, Aug. 2018.
- [29] S. Chang, B. Du, and L. Zhang, “A sparse autoencoder based hyperspectral anomaly detection algorithm using residual of reconstruction error,” in *Proc. IEEE Int. Geosci. Remote Sens. Symp.*, Yokohama, Japan, Jul./Aug. 2019, pp. 5488–5491.
- [30] X. Lu, W. Zhang, and J. Huang, “Exploiting embedding manifold of autoencoders for hyperspectral anomaly detection,” *IEEE Trans. Geosci. Remote Sens.*, vol. 58, no. 3, pp. 1527–1537, Mar. 2020.
- [31] W. Xie, J. Lei, B. Liu, Y. Li, and X. Jia, “Spectral constraint adversarial autoencoders approach to feature representation in hyperspectral anomaly detection,” *Neural Netw.*, vol. 119, pp. 222–234, Nov. 2019.

- [32] D. P. Kingma and M. Welling, "Auto-encoding variational bayes," 2013, *arXiv:1312.6114*. [Online]. Available: <http://arxiv.org/abs/1312.6114>
- [33] A. Makhzani, J. Shlens, N. Jaitly, I. Goodfellow, and B. Frey, "Adversarial autoencoders," 2015, *arXiv:1511.05644*. [Online]. Available: <http://arxiv.org/abs/1511.05644>
- [34] A. Ng, "Sparse autoencoder," CS294A Lect. Notes, Stanford, CA, USA, 2011, vol. 72, pp. 1–19.
- [35] Y. Lecun, L. Bottou, Y. Bengio, and P. Haffner, "Gradient-based learning applied to document recognition," *Proc. IEEE*, vol. 86, no. 11, pp. 2278–2324, Nov. 1998.
- [36] S. Ioffe and C. Szegedy, "Batch normalization: Accelerating deep network training by reducing internal covariate shift," in *Proc. Int. Conf. Mach. Learn.*, 2015, pp. 448–456.
- [37] R. Caye Daudt, B. Le Saux, and A. Boulch, "Fully convolutional siamese networks for change detection," in *Proc. 25th IEEE Int. Conf. Image Process. (ICIP)*, Oct. 2018, pp. 4063–4067.
- [38] D. P. Kingma and J. L. Ba, "Adam: A method for stochastic optimization," in *Proc. Int. Conf. Learn. Represent.*, 2015, pp. 1–41.
- [39] R. Basedow, D. Carmer, and M. Anderson, "HYDICE system: Implementation and performance," *Proc. SPIE*, vol. 2480, pp. 258–267, Jun. 1995.
- [40] Y. Zhong *et al.*, "Mini-UAV-borne hyperspectral remote sensing: From observation and processing to applications," *IEEE Geosci. Remote Sens. Mag.*, vol. 6, no. 4, pp. 46–62, Dec. 2018.
- [41] T. Sankey, J. Donager, J. McVay, and J. B. Sankey, "UAV lidar and hyperspectral fusion for forest monitoring in the Southwestern USA," *Remote Sens. Environ.*, vol. 195, pp. 30–43, Jun. 2017.
- [42] F. Vanegas, D. Bratanov, K. Powell, J. Weiss, and F. Gonzalez, "A novel methodology for improving plant pest surveillance in vineyards and crops using UAV-based hyperspectral and spatial data," *Sensors*, vol. 18, no. 1, p. 260, Jan. 2018.
- [43] Y. Zhong *et al.*, "MINI-UAV borne hyperspectral remote sensing: A review," in *Proc. IEEE Int. Geosci. Remote Sens. Symp. (IGARSS)*, Jul. 2017, pp. 5908–5911.
- [44] C.-I. Chang, *Real Time Progressive Hyperspectral Image Processing: Endmember Finding and Anomaly Detection*. New York, NY, USA: Springer, 2016.
- [45] C.-I. Chang, "Multiparameter receiver operating characteristic analysis for signal detection and classification," *IEEE Sensors J.*, vol. 10, no. 3, pp. 423–442, Mar. 2010.
- [46] J. M. Lobo, A. Jiménez-Valverde, and R. Real, "AUC: A misleading measure of the performance of predictive distribution models," *Global Ecol. Biogeography*, vol. 17, no. 2, pp. 145–151, Mar. 2008.
- [47] C.-I. Chang, S. S. Chiang, Q. Du, H. Ren, and A. Ifarragaerri, "An ROC analysis for subpixel detection," in *Proc. IGRSS*, Sydney, NSW, Australia, Jul. 2001, pp. 2355–2357.
- [48] X. Wang, Y. Zhong, Y. Xu, L. Zhang, and Y. Xu, "Saliency-based endmember detection for hyperspectral imagery," *IEEE Trans. Geosci. Remote Sens.*, vol. 56, no. 7, pp. 3667–3680, Jul. 2018.
- [49] S. Wang, X. Wang, Y. Zhong, and L. Zhang, "Hyperspectral anomaly detection via locally enhanced low-rank prior," *IEEE Trans. Geosci. Remote Sens.*, vol. 58, no. 10, pp. 6995–7009, Oct. 2020.



Shaoyu Wang (Student Member, IEEE) received the B.S. degree from Wuhan University, Wuhan, China, in 2017. He is pursuing the Ph.D. degree in photogrammetry and remote sensing with the State Key Laboratory of Information Engineering in Surveying, Mapping, and Remote Sensing, Wuhan University, Wuhan, China.

His major research interests include hyperspectral target detection and unsupervised learning.



Xinyu Wang received the B.S. degree in photogrammetry and remote sensing from the School of Remote Sensing and Information Engineering, Wuhan University, Wuhan, China, in 2014, and the Ph.D. degree in communication and information systems from the State Key Laboratory of Information Engineering in Surveying, Mapping and Remote Sensing (LIESMARS), Wuhan University, in 2019.

He is an Associate Research Fellow with the School of Remote Sensing and Information Engineering, Wuhan University. His major research interests range over blind source separation, hyperspectral unmixing, and target detection.



Liangpei Zhang (Fellow, IEEE) received the B.S. degree in physics from Hunan Normal University, Changsha, China, in 1982, the M.S. degree in optics from the Xi'an Institute of Optics and Precision Mechanics, Chinese Academy of Sciences, Xi'an, China, in 1988, and the Ph.D. degree in photogrammetry and remote sensing from Wuhan University, Wuhan, China, in 1998.

He was a Principal Scientist for the China State Key Basic Research Project from 2011 to 2016 appointed by the Ministry of National Science and Technology of China to lead the Remote Sensing Program in China. He is a Chang-Jiang Scholar Chair Professor appointed by the Ministry of Education of China in State Key Laboratory of Information Engineering in Surveying, Mapping, and Remote Sensing (LIESMARS), Wuhan University. He has authored or coauthored more than 700 research articles and 5 books. He is the Institute for Scientific Information (ISI) Highly Cited Author. He is the holder of 30 patents. His research interests include hyperspectral remote sensing, high-resolution remote sensing, image processing, and artificial intelligence.

Dr. Zhang is a fellow of the Institution of Engineering and Technology (IET). He was a recipient of the 2010 Best Paper Boeing Award, the 2013 Best Paper ERDAS Award from the American Society of Photogrammetry and Remote Sensing (ASPRS), and the 2016 Best Paper Theoretical Innovation Award from the International Society for Optics and Photonics (SPIE). His research teams won the top three prizes of the IEEE GRSS 2014 Data Fusion Contest, and his students have been selected as the winners or finalists of the IEEE International Geoscience and Remote Sensing Symposium (IGARSS) Student Paper Contest in recent years. He also serves as an Associate Editor or Editor for more than ten international journals. He is the Founding Chair of the IEEE Geoscience and Remote Sensing Society (GRSS) Wuhan Chapter. He is serving as an Associate Editor for the IEEE TRANSACTIONS ON GEOSCIENCE AND REMOTE SENSING.



Yanfei Zhong (Senior Member, IEEE) received the B.S. degree in information engineering and the Ph.D. degree in photogrammetry and remote sensing from Wuhan University, Wuhan, China, in 2002 and 2007, respectively.

Since 2010, he has been a Full professor with the State Key Laboratory of Information Engineering in Surveying, Mapping and Remote Sensing (LIESMARS), Wuhan University, China. He organized the Intelligent Data Extraction, Analysis and Applications of Remote Sensing (RSIDEA) Research Group.

He has authored or coauthored more than 100 research articles in international journals, such as *Remote Sensing of Environment*, *ISPRS Journal of Photogrammetry and Remote Sensing*, the IEEE TRANSACTIONS ON GEOSCIENCE AND REMOTE SENSING. His research interests include hyperspectral remote sensing information processing, high-resolution remote sensing image understanding, and geoscience interpretation for multisource remote sensing data and applications.

Dr. Zhong is a fellow of the Institution of Engineering and Technology (IET). He was a recipient of the 2016 Best Paper Theoretical Innovation Award from the International Society for Optics and Photonics (SPIE). He won the Second-Place Prize in 2013 IEEE GRSS Data Fusion Contest and the Single-View Semantic 3-D Challenge of the 2019 IEEE GRSS Data Fusion Contest, respectively. He is serving as an Associate Editor for the IEEE JOURNAL OF SELECTED TOPICS IN APPLIED EARTH OBSERVATIONS AND REMOTE SENSING, and the *International Journal of Remote Sensing*.